atmosphere

MDPI

Article

Daily Rainfall Patterns During Storm "Daniel" Based on Different Satellite Data

Stavros Kolios * and Niki Papavasileiou

Department of Aerospace Science and Technology, Faculty of Sciences, National Kapodistrian University of Athens (NKUA), 34400 Psachna, Greece; npapavas@di.uoa.gr
* Correspondence: skolios@aerospace.uoa.gr; Tel.: +30-22280-21872

Abstract: Extreme rainfall from a long-lived weather system called storm "Daniel" occurred from 4th to 11th September 2023 over the central and eastern Mediterranean, leading to many devastating flood events mainly in central Greece and the western coastal parts of Libya. This study analyzes the daily rainfall amounts over all the affected geographical areas during storm "Daniel" by comparing three different satellite-based rainfall data products. Two of them are strictly related to Meteosat multispectral imagery, while the other one is based on the Global Precipitation Measurement (GPM) satellite mission. The satellite datasets depict extreme daily rainfall (up to 450 mm) for consecutive days in the same areas, with the spatial distribution of such rainfall amounts covering thousands of square kilometers almost during the whole period that the storm lasted. Moreover, the spatial extent of the heavy rainfall patterns was calculated on a daily basis. The convective nature of the rainfall, which was also recorded, characterizes the extremity of this weather system. Finally, the intercomparison of the datasets used highlights the satisfactory efficiency of the examined satellite datasets in capturing similar rainfall amounts in the same areas (daily mean error of 15 mm, mean absolute error of up to 35 mm and correlation coefficient ranging from 0.6 to 0.9 in most of the examined cases). This finding confirms the realistic detection and monitoring of the different satellite-based rainfall products, which should be used for early warning and decision-making regarding potential flood events.

Keywords: Meteosat; hydrology satellite application facilities; storm Daniel; satellite-based rainfall data; GPM

check for updates

Citation: Kolios, S.; Papavasileiou, N. Daily Rainfall Patterns During Storm "Daniel" Based on Different Satellite Data. *Atmosphere* **2024**, *15*, 1277. https://doi.org/10.3390/atmos15111277

Academic Editor: Mario Marcello Miglietta

Received: 11 September 2024
Revised: 21 October 2024
Accepted: 21 October 2024
Published: 25 October 2024

Copyright: © 2024 by the authors. Licensee MDPI, Basel, Switzerland. This article is an open access article distributed under the terms and conditions of the Creative Commons Attribution (CC BY) license (https://creativecommons.org/licenses/by/4.0/).

1. Introduction

Climate change is causing important shifts in rainfall patterns, including changes in both the frequency and severity of precipitation, which increase the risk of floods. According to the IPCC's 6th assessment report [1], climate change will continue to increase excessive precipitation and flooding in many parts of Europe [1–8]. Furthermore, it is mentioned that, considering a continuous increase in the global temperature due to climate change, floods worldwide will be a more frequent source of huge socio-economic impact, as has already been recorded in many studies [2–5]. According to the World Health Organization (WHO), floods affected more than 2 billion people worldwide between 1998 and 2017. The severity of floods is also expected to become more devastating for human lives and infrastructure in the near future [1].

This trend was recently confirmed by extreme weather events like storm "Daniel", which caused human losses as well as substantial property and infrastructure damage due to heavy rainfall-induced flooding. Analyzing events like storm "Daniel" is crucial for understanding the impacts of climate change on flood events and their causes. Such analyses provide valuable insights into how precipitation patterns can cause flood events in a rapidly changing climate, aiding in the development of strategies that enhance resilience and preparedness for future extreme weather events. Moreover, the increasing frequency and intensity of extreme precipitation events underscores the urgent need for proactive measures to adapt to the impacts of climate change and mitigate the risks associated with flooding [1–8].

To evaluate spatiotemporal dynamics and the hydrological processes involved in flood event analysis, a wide range of data sources and approaches are typically used, including ground-based meteorological networks, weather radars, satellite observations, and multiple model simulations [9,10].

At this point, it is worth pointing out that ground-based meteorological networks, although providing real measurements of rainfall, are location-specific and a significant economic cost is often needed for the maintenance of such networks. Thus, they do not provide sufficient information about the spatial extent of the rainfall because, in most cases, these networks are not well dispersed and do not have a sufficient number of operational stations. On the other hand, satellite-based datasets often underestimate/overestimate the amount of rainfall because of the difficulty of capturing localized rainfalls in mountainous or coastal regions. Nevertheless, advances in satellite instrumentation (improvements in the spatial, temporal and spectral resolution), as well as the use of modern algorithms, especially Artificial Neural Networks (ANNs), have already proved very important in providing reliable rainfall estimates and relative data products.

The well-known issues associated with traditional ground-based meteorological networks and the ability of alternative solutions to efficiently capture not only the rainfall amount but also the rainfall patterns promote the increasing use of alternative instrumentation such as weather radars, satellites and models to estimate the amount of rainfall along with the spatial extent. For example, in a work by Meyer J. et al., 2021 [9], a radar-based precipitation climatology (RADKLIM) dataset was used to create a precipitation database along with ERA5 atmospheric reanalysis data from the Copernicus Climate Data Store (CDS) to investigate the temporal variability in rainfall and its link with floods [10]. In another recent study, Ludwig P. et al., 2023 [10], focused on the extraordinary flood event of July 2021 in Central Europe. The analysis included precipitation data from many different sources as well as model simulations [9]. These findings highlight the value of using multi-disciplinary techniques in flood event research, allowing for a more thorough understanding of flood mechanisms. Moreover, recent studies that utilize satellite observations have incorporated precipitation estimates from satellites with a spatial resolution of $0.25^\circ \times 0.25^\circ$ [11,12] and a temporal resolution of 3 h into hydrological modeling, enabling the near-real-time monitoring of precipitation [11]. Other research has integrated passive microwave (PMW) and infrared (IR) bands and merged these rainfall estimates with gauge data to further enhance accuracy and reliability [13–18].

Indeed, satellite observations play a crucial role in flood monitoring and forecasting due to their ability to provide the continuous and full coverage of rainfall patterns [13,16,19–22]. To achieve accurate rainfall estimates, a combination of IR and passive PMW satellite channels is often utilized [13–17]. This strategic approach strikes a balance between spatial and temporal analysis, enabling continuous monitoring and providing precise rainfall estimates [13]. These observations offer valuable insights into rainfall distribution across large regions, aiding in the identification of areas susceptible to heavy rainfall and flooding. By offering real-time information on precipitation intensity and the geographical extent, satellite data significantly enhance flood forecasting and early warning systems. The integration of satellite observations with various models, such as hydrological models, is essential for generating comprehensive, accurate, and valuable conclusions [21,22]. This approach enhances the depth and precision of insights, fostering a clearer understanding and facilitating more informed decisions. Additionally, it supports improved risk assessment and mitigates the potential impacts on populations and infrastructure.

At this point, it is worth mentioning that although satellite-based rainfall products are widely used today and offer real-time monitoring, they have limitations such as resolution issues, the underestimation or overestimation of rainfall [23,24], and difficulties capturing localized rainfall in mountainous or coastal areas [25]. However, modern satellites have significantly improved their spatial, spectral, and temporal resolution, surpassing even high-resolution weather models. The studies in [23–28] are some characteristic examples of accuracy assessments, demonstrating their ability to provide highly accurate rainfall estimates.

This study underscores the importance of using satellite-based rainfall data products to efficiently capture both rainfall amounts and their spatial extent during the intense storm "Daniel" (case study analysis), which caused extended periods of heavy rainfall and large flood events across central and eastern parts of the Mediterranean basin. In contrast to many prior studies that incorporate ground-based datasets [1,7,8,26–28], this study exclusively uses three satellite-based rainfall products: HSAF61, the MRP method for rain estimates using SEVIRI data, and the GPM IMERG product. This approach relies entirely on satellite observations, ensuring a consistent and uniform estimation of rainfall. The rainfall was studied on a daily basis, with particular emphasis on the extreme nature, duration, and convective processes involved in the storm, allowing for a thorough analysis of the storm's overall impact (Figure 1). An intercomparison was also conducted to identify the similarities and differences in rainfall estimates during this extreme weather event. Furthermore, this study highlights the significance of satellite-based rainfall datasets for flood risk management and early warning systems. Beyond examining the synoptic conditions that led to the storm, the focus on convective rainfall patterns provides a critical insight into the role of convection in intensifying the storm's effects.

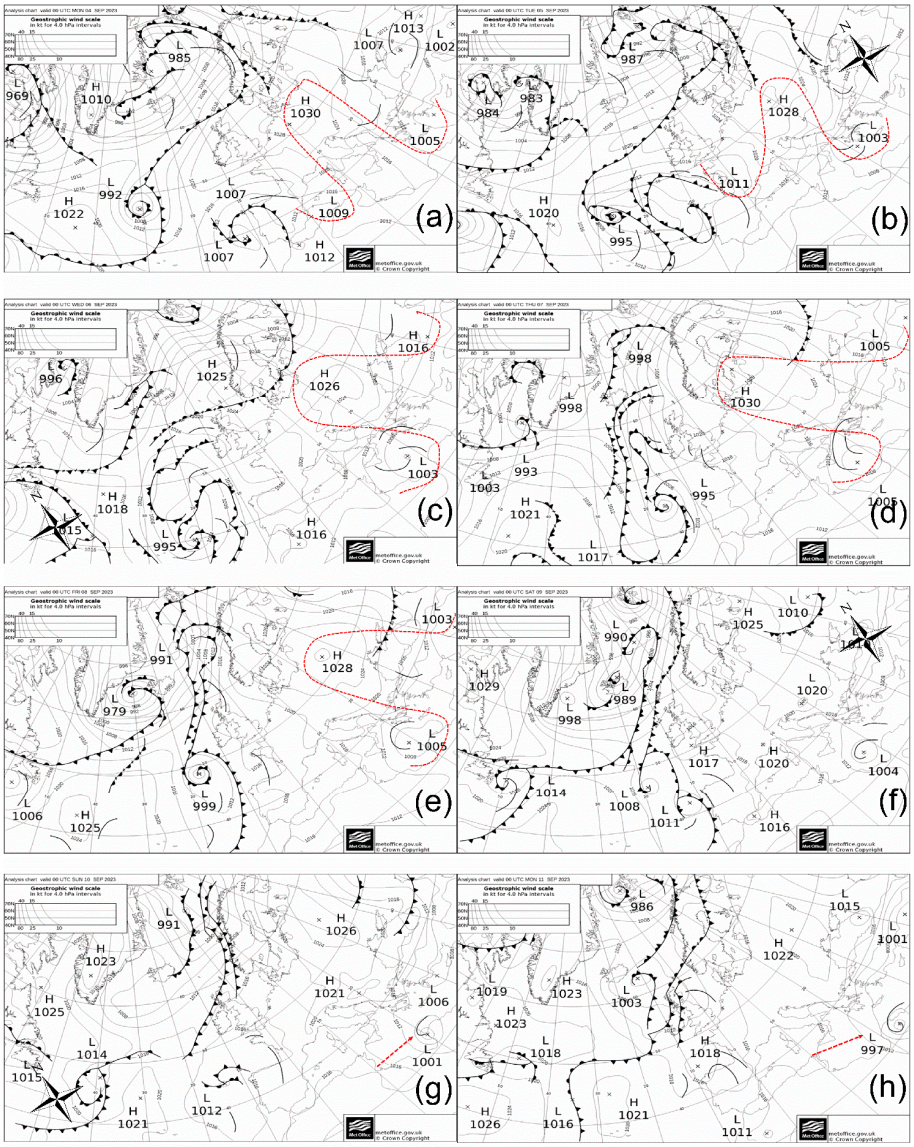


Figure 1. Daily surface weather maps from 4–11 September 2023 (**a**–**h**) across Europe. The red dashed curves represent the Omega blocking atmospheric conditions during the first five days, while the next ones show the barometric low that existed north of Libya (red arrow) in the Mediterranean Sea.

2. Data and Methods

In this section, the synoptic conditions that led to extreme floods, especially in Greece (Thessaly Prefecture) and Libya (western coastal areas), are described. In addition, all the datasets used and the analytical methodologies are presented below.

2.1. Synoptic Analysis

At the end of August and in the first days of September 2023, a persistent low-pressure pattern, known as omega blocking, was established initially over Central Europe, causing the formation of low-pressure centers in the Mediterranean and over the Iberian Peninsula. On 4th September, the low-pressure surface systems across Europe created a deep trough, originating over eastern Europe and developing between two massive ridges over Central Europe and the Middle East (Figure 1). This synoptic condition, known as "Omega blocking", began gradually to move southwards over the Balkan peninsula.

During the first day of this persistent extreme atmospheric condition (red dashed line in Figure 1), organized cloud convection occurred (Figure 2) in eastern parts of Bulgaria (near Black Sea) and Turkey (greater area of Istanbul), where the first severe impacts on properties and humans were recorded [29].

The next day (5th September2024), this synoptic condition caused a predominantly easterly–northeasterly flow over mainland Greece, bringing warm, humid, and conditionally unstable air from the Aegean Sea against the mountains of central Greece and Thessaly (part of the Pindos Mountain ridge). The trough remained quasi-stationary, and the cloud convection persisted in extended areas of Bulgaria and Turkey (Figure 2a,b), causing small-scale flash floods but resulting in extensive damage to private properties and infrastructures and human losses. On 6th September 2023, as evolutional part of the same large-scale atmospheric condition (Figure 1c), a Mediterranean Cyclone (the medicane called "Daniel") started to develop over the Ionian Sea, south-west of the Peloponnesus (Greece). Due to the occlusion of the cold sector of the front, thunderstorms accompanied by heavy showers and torrential rainfall impacted these areas, but primarily the central part of Greek peninsula and the greater area of the Thessaly Prefecture (Figure 2c). It was reported that, during the passage of this storm from Greece, there were 17 casualties and significant damage was caused to the agricultural sector, ranging from approximately 10% to 50% in different areas, with an overall financial loss of EUR 2 billion [4,29].

Over the next two days (especially in the afternoon of 7th September), the medicane "Daniel", which had impacted Greece, gradually shifted south towards the Ionian Sea. At this point, it is worth mentioning that, although the Mediterranean Sea does not have tropical cyclones or hurricanes, there are some cases, such as this one, where the low-pressure systems can produce a structurally similar formation to tropical storms. These weather formations are characterized by violent rotating winds close to the cyclone's center and many deep mesoscale convective systems with intense lightning activity and heavy rainfalls.

As the studied cyclone approached the central Libya and its eastern coast late on 9th September (Figure 1f), it was enriched with huge amounts of humidity over the Mediterranean. In parallel, the system experienced a temporary stall in its east–southeastward progression and lingered for almost 24 h above the aforementioned coastal regions (Figure 1g). This slowdown of the medicane (Figure 1h) caused persistent and intense thunderstorms to perpetually hit the same area, dumping huge amounts of cumulative precipitation daily, over 240 mm, and resulting in the destruction or damage of 10−20% of properties and infrastructure and almost 6000 casualties [5,6].

The occurrence of organized cloud convection ("CC") during the studied period (4–11 September 2023) was recorded, resulting in thematic maps showing the daily frequency of occurrence of CC based on Meteosat imagery (Figure 2).

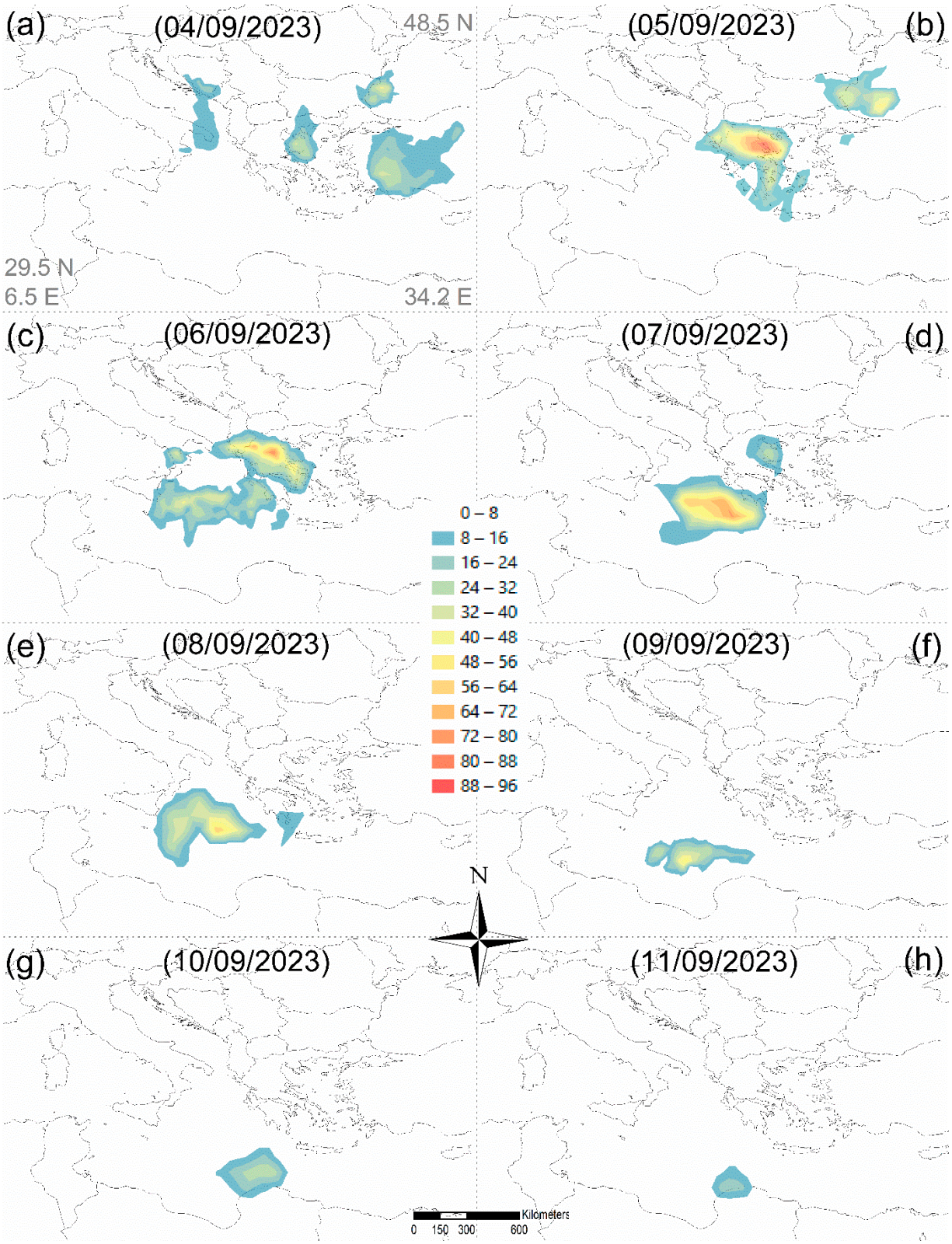


Figure 2. Thematic maps showing the daily frequency of the occurrence of cloud convection ("CC") based on Meteosat imagery. The classes in the legend represent the number of timeslots (unitless) with CC (the maximum number is "96", representing the total number of available timeslots per day according to the Meteosat temporal resolution).

More specifically, the pixels that are characterized as convective were detected for each of the available Meteosat images and then summarized on a daily basis. The criteria used for this characterization are presented in the study of Kolios, 2023 [30]. It is noted that the maximum pixel value is "96" (Figure 2), representing the total number of available timeslots per day according to the Meteosat nominal temporal resolution.

In Figure 2, during the first three days, it can be clearly seen that across the greater area of central Greece, and more specifically in the Thessaly Prefecture, the cloud convection was present almost all day (pixel values greater than "72" correspond to a duration of convective occurrence above 18 h), particularly on 5th and 6th September 2023 (Figure 2b,c). At this point, it is worth mentioning that during the first two days (Figure 2a,b), convection was present in parts of Bulgaria and Turkey, with a duration of about half a day, which is clearly above the usual lifetime (typically 2–4 h) of a mesoscale convective cloud system [31]. As mentioned above, on 6th September 2023, the cloud convection shifted to the Ionian Sea as part of the active low-pressure system (medicane "Daniel"). Although this system was quasi-stationery and persistent over time, it started to dissipate slowly. Despite the significantly smaller and short duration of CC on 10th and 11th September (Figure 2g,h), the cloud convective pattern, along with the stratiform cloudiness (rich in humidity due to its previous and long-lasting existence over the Ionian Sea) that accompanied it, caused heavy rainfall (and extreme flooding) along the western coastline of Libya (greater area of Derna city).

2.2. Datasets

During the study period (4–11 September 2023) of storm "Daniel", three different satellite-based rainfall products were used to capture and analyze the extremity and the duration of the entire weather event. These rainfall products were chosen because they are based exclusively on satellite remote sensing recordings from various instruments, satellites and spectral regions ranging from infrared to microwave. Additionally, an intercomparison among the used satellite-based rainfall products was conducted to highlight the role of such products in accurately capturing rainfall patterns and amounts, as well as the degree of concurrence in different satellite-based rainfall estimates.

The first dataset is the HSAF H61B precipitation product, which provides accumulated precipitation data at the ground level by blending microwave (MW) and infrared (IR) measurements. This near-real-time product integrates precipitation estimates from the 10.8 μm channel of the SEVIRI instrument and the precipitation from microwave sensors [32].

The second dataset is the precipitation product from the GPM satellite (GPM—IMERG: "Global Precipitation Measurement Mission—Integrated Multi-satellitE Retrievals", version 6. The GPM—IMERG precipitation product was developed to provide near-real-time, high-resolution and global precipitation estimates by combining data from various passive and microwave (PMW) satellite sensors [33]. For the needs of the study, daily accumulated datasets with a spatial resolution of 0.1 degree [33,34] were used.

The third dataset is the satellite-based rainfall product described in detail in the study by Kolios et al., 2022 [35], and originates from the operational use of the MeCoSA algorithm [30]. This product (hereinafter: MeCoSa Rainfall Product or "MRP") is based on Meteosat Second Generation (MSG) multispectral imagery, having the same spatial and temporal resolution as MSG satellite data. The MRP utilizes four bands of the Spinning Enhanced Visible and Infrared Imager (SEVIRI) onboard the MSG satellite [35]. The algorithm is primarily designed to detect and nowcast cloud convection, which is crucial for identifying intense rainfall events and severe weather conditions. It should be noted that this rainfall product has already been evaluated for its accuracy at the regional scale using ground measurements of a network of seven meteorological stations [35]. For the needs of the study, the calculated rain rate was converted to the daily accumulated rainfall by summarizing the hourly totals.

At this point, it must be noted that all the used rainfall products were clipped around the same geographical borders and resampled to obtain the same spatial resolution, ensuring comparability at the pixel level (common pixel size: 0.05 decimal degrees). This spatial

resolution is very close to the initial spatial resolution of the HSAF (H61B) and MRP rainfall products, but is twice as fine as the initial one in the GPM (IMERG) product. Although this resampling procedure introduces a small distortion of the initial pixel values, it allows their comparison at the pixel basis, retaining the order of magnitude of the estimated rainfall amounts satisfactorily. The nearest neighbor approach was chosen to resample the datasets because it causes the smallest changes in the initial values on a pixel basis. Also, it must be mentioned that although these data can be found in finer temporal resolution, it was decided that they would be analyzed on a daily basis. The reason for this choice is that this study tries to underscore the extremity of this storm by underscoring the accumulated rainfall amounts and the large areas that were covered with heavy rainfall, which was a major component of the devastating floods during storm "Daniel". Instantaneous rainfall is very important in flash floods, but in this studied case, the main characteristic was persistent heavy rainfall over large areas for consecutive days, which overloaded the hydrographic network and caused extensive floods. Also, it is noted that HSAF H61B and the GPM—IMERG are two well-known and widely used worldwide precipitation products with high accuracy and large geographic coverage [32,33,36]. The MRP product is a new precipitation product that has been already tested [35] and has the same spatial resolution as H61B.

3. Results

To analyze the examined extreme weather event in terms of the rainfall produced, as mentioned above, three different satellite rainfall products and their intercomparison were tested (Figure 3). More specifically, Figure 3 presents the daily scatterplots for all the pairs of rainfall products, along with their corresponding boxplots.

By examining the scatterplots for each day (Figure 3), a satisfactory correlation among them in most of these cases can be observed. The diagonal (blue solid lines) in all the scatterplots in Figure 3 indicates the overestimation/underestimation between all the pairs of data on a daily basis. Figure 3 shows that in most of the cases, the largest divergence in the correlation of the pairs of values is evident, especially in the extreme rainfall values; however, overall, there is quite satisfactory accuracy (Figure 4c). Moreover, the large dispersion (large range of distribution of values) is strong evidence of the capability of the examined rainfall products to capture extreme rainfall. From the scatterplots and the corresponding boxplots in Figure 3, it appears that the HSAF (H61B) and MRP rainfall values are more dispersed than GPM (IMERG), especially in the highest parts of the distributions, which indicates a high sensitivity in capturing heavy rainfall at the pixel level.

Additionally, the basic descriptive statistics for all the value distributions in Figure 2 are presented in Table 1. This table provides statistics about all the common rainy pixel values in each day. Characteristically, the third quantile of the distribution ($P_{75\%}$) in most of the cases shows a daily rainfall amount above 40 mm, which highlights the extremity of the phenomenon. Moreover, the percentile of $P_{95\%}$ also shows extreme daily rainfall during the whole examined period, over large areas of many thousands of square kilometers (each pixel has 0.05 degrees dimensions).

In Figure 4, the daily Correlation Coefficient (CC), Mean Error (ME) and Mean Absolute Error (MAE) are presented. The correlation values for all these comparisons are quantitatively presented in Figure 4a. In this Figure, it can be seen that the lowest correlation coefficients are for HSAF (H61B) and the GPM (IMERG) comparisons. Low correlation coefficients are observed between the MRP and GPM (IMERG) rainfall products in the comparison, too. Nevertheless, these low correlation values are found only on days where the rainfall has a low and narrow range of value distributions. In all other cases, the correlation coefficient of these pairs of data ranges between 0.5 and 0.8 (Figure 4a). For the HSAF (H61B) and MRP rainfall products, which come from the same satellite (Meteosat) and have the same spatial resolution, the correlation coefficients are relatively high as they range between 0.6 and 0.9. Conclusively, according to Figure 4c, the CC exceeds 0.6 in 70% of all the cases, which generally shows a quite satisfactory correlation among the examined rainfall products, considering the fact that the examined rainfall products are significantly different.

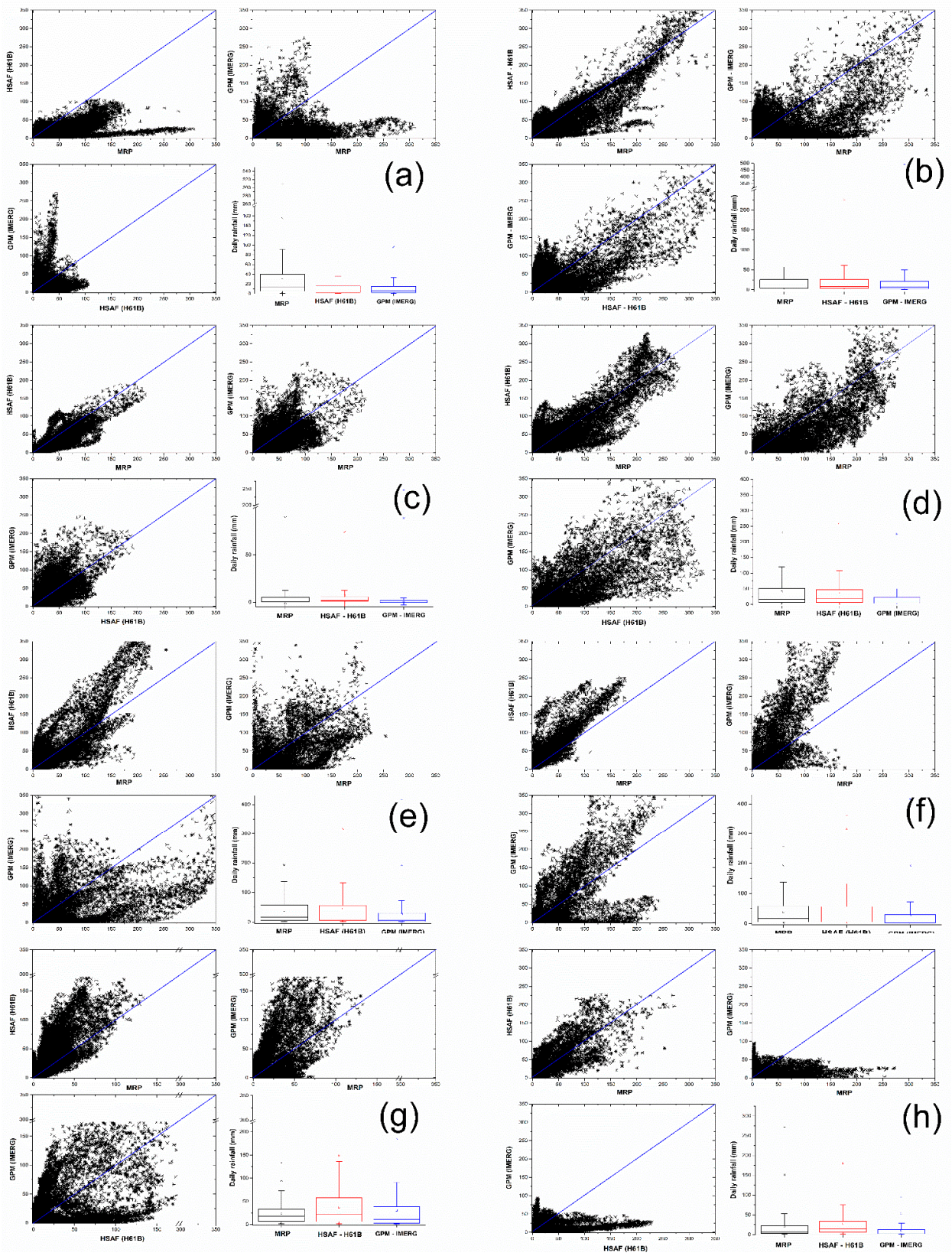


Figure 3. Scatterplots that represent the comparisons on pixel-bases among the three different rainfall data products from the first day on 4 September 2024 to the last day 11 September 2024 (**a**–**h**) during the examined period. The relative boxplots of the daily distributions of these rainfall data products, are also provided (black: "MRP", red: "HSAF-H61B", blue: "GPM-IMERG").

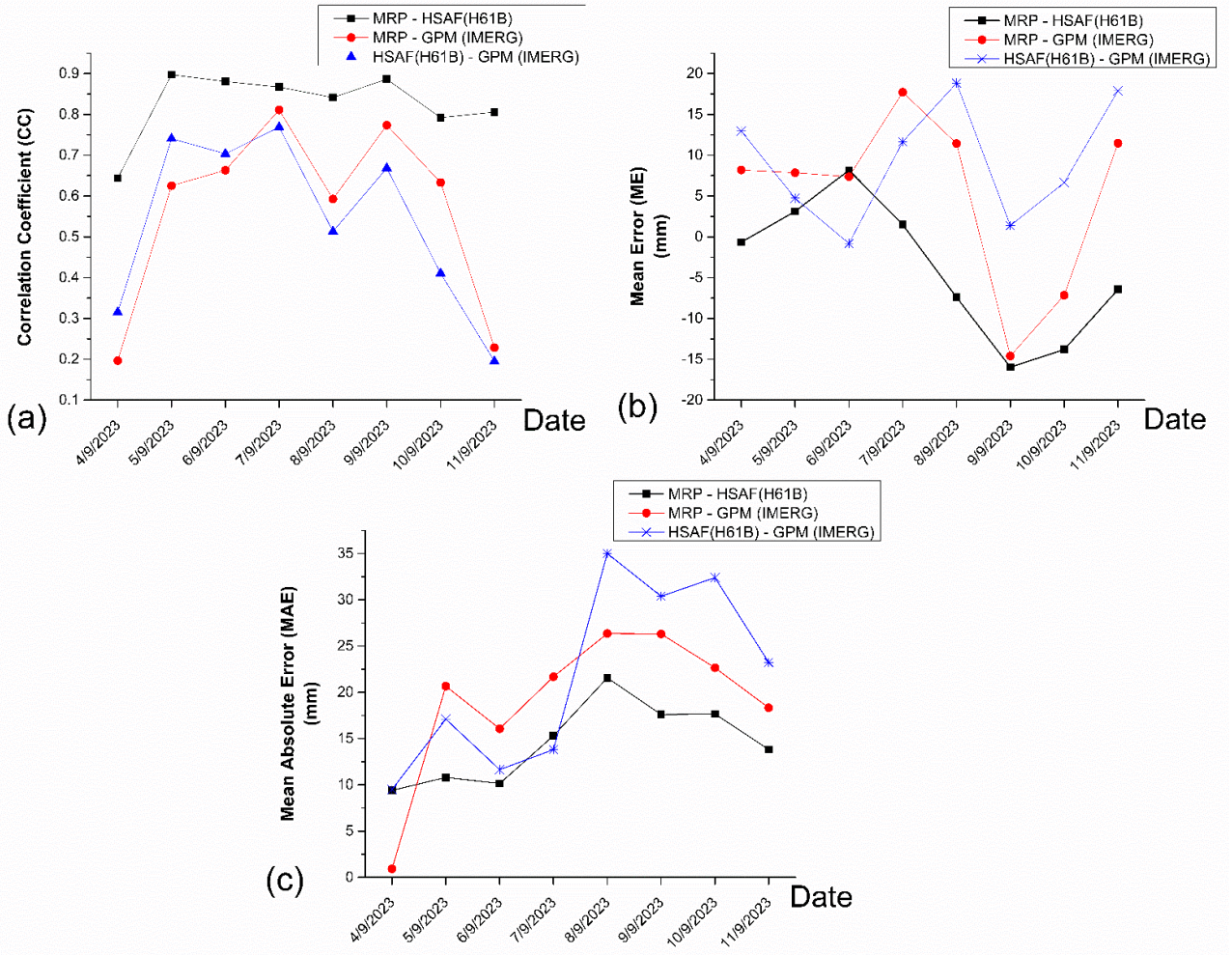


Figure 4. Daily values of (**a**) Correlation Coefficient, (**b**) Mean Error (ME), and (**c**) Mean Absolute Error (MAE) among the pairs of examined datasets on a pixel basis.

According to Figure 4b, where the Mean Errors (MEs) are presented, there is a systematic underestimation of the MRP rainfall values in comparison to the HSAF (H61B) values, ranging from 1 to 15 mm. In the same figure, the other two comparisons show large variations. More specifically, the MRP–GPM (IMERG) comparisons reveal the overestimation of the MRP rainfall values relative to the GPM (IMERG) values, ranging from 7 to 15 mm in most cases. Similar results were observed between the HSAF (H61B) and GPM (IMERG) rainfall values. Although the ME values are notable (ranging from 7 to 25 mm in most of the examined cases), this type of error remains one order of magnitude lower than the extreme rainfall values recorded. This is sufficient to characterize the satisfactory accuracy of all these datasets when quantitatively determining the intensity and the extremity of the studied weather events, despite their divergences at the pixel level. Although the ME values seem to be relatively high in most of the examined cases (Figure 4b), it should be noted that they are very low relative to the extreme rainfall values recorded, as well as the standard deviation values of their distributions. Thus, these ME values can be characterized as quite satisfactory, considering the large disparities in the rainfall values and the different natures of the examined rainfall products.

Regarding the Mean Absolute Error (MAE), which is provided in Figure 4c, the lowest values are again observed in the HSAF (H61B)–MRP pairs of values, ranging from 7.0 to 20 mm. This range can be considered satisfactory, especially given that 25% of pixels have values that are two or more times higher than the relative MAE. The MAE values for the MRP–GPM (IMERG) pairs are similar but slightly higher, reaching up to 25 mm,

as can be seen in Figure 4c. The largest variation in MAE values is observed in the HSAF (H61B)–GPM (IMERG) pairs, with the worst case reaching 35 mm (Figure 4c). At this point, it should be noted that although the MAE values are notable (ranging from 7 to 25 mm in most of the examined cases), this type of error remains one order of magnitude lower than the extreme rainfall values recorded. This result is sufficient to characterize the accuracy of all these datasets when quantitatively determining the intensity and the extremity of the studied weather events, despite their divergences at the pixel level.

Table 1. Descriptive statistics of the daily distributions for the three different rainfall products used in this study.

Date	Rainfall Product	N (Total Number of Common Rainy Pixels)	Mean (mm)	Standard Deviation (mm)	Median (mm)	Maximum (mm)	Interquartile Range (mm)	$P_{75\%}$ (mm)	$P_{95\%}$ (mm)
4 September 2023	MRP	38,301	29.69	37.19	13.27	308.89	34.37	39.77	107.82
	HSAF	38,301	12.00	14.01	6.79	106.78	13.57	15.99	40.57
	GPM	38,301	12.76	19.88	5.89	273.75	12.46	14.92	46.50
5 September 2023	MRP	39,989	26.95	45.68	9.34	334.50	21.14	25.45	127.69
	HSAF	39,989	23.83	41.63	8.21	392.33	23.04	26.49	95.38
	GPM	39,989	19.10	33.41	7.06	491.20	18.78	21.39	74.72
6 September 2023	MRP	30,909	26.88	27.41	17.25	214.45	32.34	39.00	81.96
	HSAF	30,909	18.71	22.46	10.22	191.21	20.99	24.92	66.01
	GPM	30,909	19.52	28.48	7.42	246.61	20.48	23.39	79.32
7 September 2023	MRP	23,766	40.65	54.33	16.69	280.86	45.49	51.26	174.85
	HSAF	23,766	39.15	53.53	19.20	327.58	40.97	46.80	161.51
	GPM	23,766	25.34	45.75	7.32	389.53	18.74	21.78	127.12
8 September 2023	MRP	16,086	38.18	46.18	16.61	255.52	52.83	57.91	139.79
	HSAF	16,086	45.59	64.96	19.85	361.52	50.71	55.94	191.26
	GPM	16,086	26.75	44.84	5.30	416.32	27.86	30.22	130.08
9 September 2023	MRP	10,980	25.67	31.73	10.81	178.08	31.91	36.28	94.44
	HSAF	10,980	41.64	49.51	22.58	253.80	50.37	56.64	157.19
	GPM	10,980	40.26	66.00	11.78	427.91	36.96	39.73	193.34
10 September 2023	MRP	10,022	23.31	21.25	17.41	133.07	26.30	33.19	66.76
	HSAF	10,022	37.11	38.58	21.61	235.31	51.89	58.11	120.09
	GPM	10,022	30.47	42.54	10.83	267.44	35.23	38.25	126.85
11 September 2023	MRP	11,995	21.24	33.32	6.28	271.76	20.15	22.79	98.21
	HSAF	11,995	27.67	35.42	14.03	227.93	27.54	33.70	105.77
	GPM	11,995	9.77	11.35	5.40	94.54	10.47	12.84	33.12

The following Figure (Figure 5) depicts the daily rainfall patterns where the daily values exceeded 50 mm simultaneously for all three satellite-based products (green-colored areas). This choice was based on the effort to emphasize the extremity of the phenomenon that produced heavy rainfall for many consecutive days over large areas. It is also mentioned that the threshold of 50 mm is considered sufficient to characterize heavy rainfall [37–39]. Furthermore, the common pixels with daily rainfall amounts ranging from 25 mm to 50 mm are also presented (orange-colored areas). Figure 5 highlights the long duration of the heavy rainfall (daily values higher than 500 mm) and its extensive continuous patterns that overloaded the hydrographic network and, at the final stage, caused devastating floods. As can be seen from Figure 5a, only a small rainfall pattern was observed in the Black Sea on 4 September 2023; meanwhile, the next day, as the cyclonic system started to intensify, a mesoscale rainfall pattern with a daily accumulated rainfall above 50 mm and an areal extent of 6.460 km^2 (common area for all the examined datasets) could be seen, as shown in Figure 5b. On the same day (5 September 2023), a large rainfall pattern with a total extent of 24.427 km^2 occurred over central Greece (the greater area of Thessaly Prefecture). Extensive areas with a daily rainfall exceeding 50 mm were also recorded over the next two days (Figure 5c,d). The heavy rainfall that occurred for three consecutive days in Thessaly

Prefecture caused the largest and most catastrophic flood event in Greece's history. In the following two days, the cyclonic activity shifted over the Ionian Sea, and most of the heavy rainfall occurred over the sea.

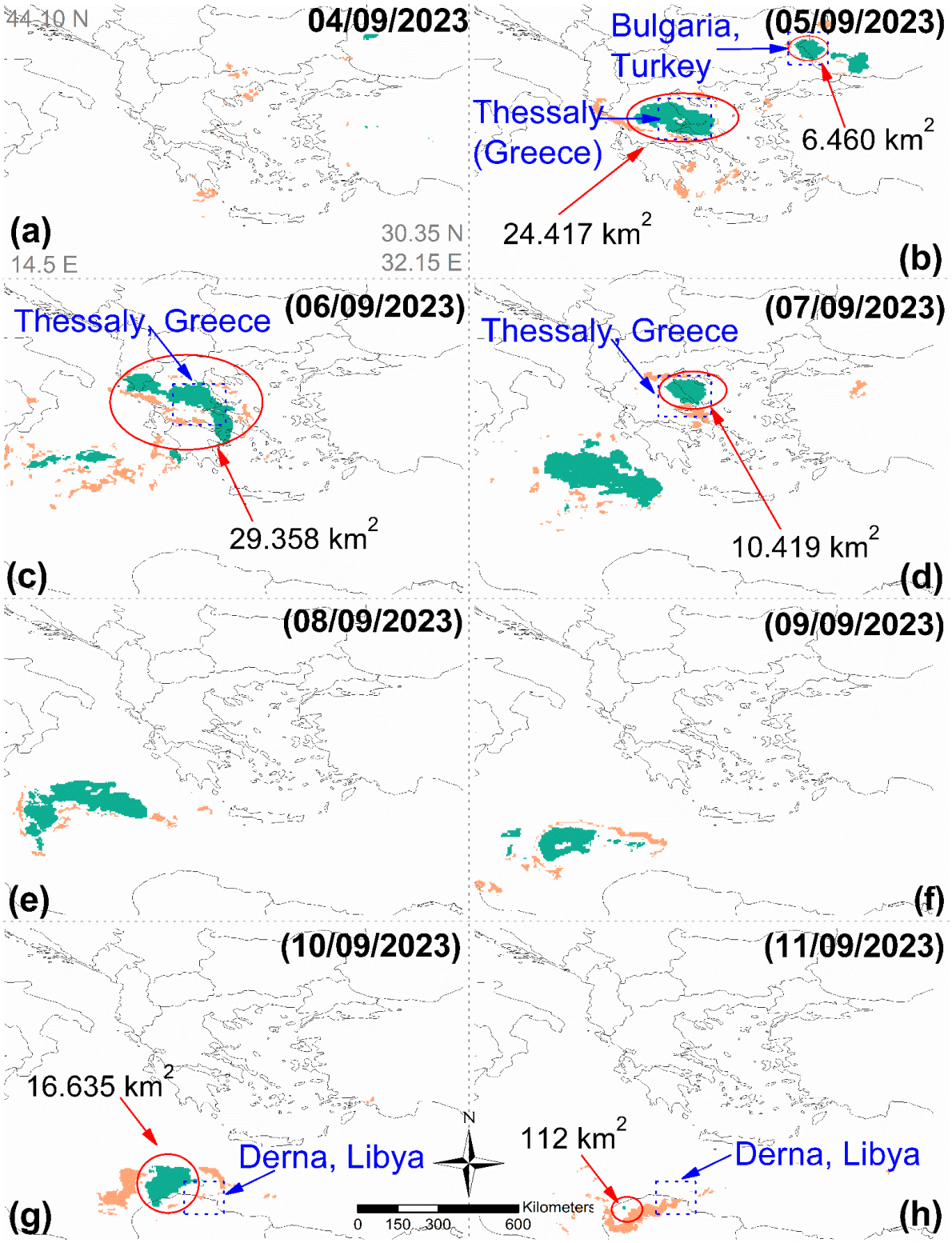


Figure 5. Rainfall patterns exceeding 50 mm (green-colored areas) and ranging from 25 mm to 50 mm (orange-colored areas). The daily patterns are the common pixels of all the examined rainfall datasets.

On 10 September 2023, the cyclonic activity continued near the Libyan coastline, mainly westerly but very close to the city of Derna where severe flooding occurred. Figure 5g depicts a large area (16.635 km^2) with a daily rainfall amount exceeding 50 mm (common for all the examined rainfall products). Nevertheless, only a small part of this area was over the Libyan coastline (925 km^2). This small area of inland rainfall pattern, which was efficiently recorded from satellite-based data, seemed to experience a cumulative rainfall of 240 mm (up to 414 mm in the city of Al-Bayda), as recorded from ground-based stations; this was referred to in a recent study by Normand and Heggy, 2024 [6]. Over the city of Derna, the daily rainfall was found to range from 25 to 50 mm (orange-colored pixels). On the next day (11 September 2023), Figure 5h shows only a small area of heavy rainfall in the greater area, with the extent being in the lowest limits of the mesoscale (i.e., 112 km^2) and not convective in nature (Figure 2h), while the daily rainfall pattern over Derna ranged again from 25 mm to 50 mm; however, it is mentioned again that this is the common area of the three examined rainfall products and not the actual rainfall recorded by them. According to these findings, it seems that the notable daily rainfall just over Derna city could be also produced from the stratiform cloud regions, which are also humid, produce rainfall, are usually located around the active convection (Figure 2g,h), and could also cause significant flood episodes in combination with other favorable conditions such as the topography and the land cover.

4. Discussion and Conclusions

This study analyzes the daily rainfall patterns that caused devasting floods in Turkey, Bulgaria (areas along the coastline of the Black Sea) and Greece and Libya from 4 September 2023 to 11 September 2023 during the extreme weather event widely known as storm "Daniel". The rainfall was examined by using and comparing three different satellite-based rainfall data products in order to underscore the crucial role of such datasets in capturing extreme rainfall amounts as well as their spatial extent, which can significantly contribute to flood events. Initially, when focusing on the phenomenon, cloud convection, which is the main factor behind heavy rainfall, was examined. The cloud convection was depicted in terms of the frequency of convective occurring in Meteosat satellite imagery and by using the MeCoSa algorithm [30]. It was found that there was long-lasting daily convection (reached up to 18 h (5th and 6th September 2023) with a large areal extent (thousands of km^2). This persistent cloud convection over large areas for many hours per day (Figure 2), caused continuous heavy rainfall (convective nature of rainfall), gradual surface water accumulation and finally large floods. This was evident in the case of the Thessaly Prefecture [29].

Regarding the daily rainfall amounts recorded by different satellite products, it was found that all the different rainfall products used in this study recorded high amounts of daily rainfall over the same areas and were generally in good agreement (Figures 3 and 4 and Table 1). A main finding is that in almost 70% of all the daily comparisons (5 days), the correlation coefficients (CCs) exceed 0.6, while there are many cases with a CC between 0.8 and 0.9. At this point, it must be mentioned that the examined statistical metrics, except the comparison of the rainfall values on a pixel basis, actually include their spatial comparison, too. So, the scores in all the statistical parameters of Figure 4 can be considered to have satisfactory accuracy because, in both the rainfall amounts and the spatial patterns of rainfall, relatively small divergencies were found. These findings could be notable conclusions in terms of the capability of different satellite-based rainfall products to capture similar rainfall amounts during extreme rainfall events. Moreover, their unique capability to depict the spatial distribution of the rainfall amounts could not only significantly help in studying such phenomena, but also in improving decision-making and planning to prevent fatalities and damage to infrastructure and the agricultural sector.

The heavy rainfall on a daily basis was analyzed using a common threshold value of 50 mm (Figure 5) and a second one between 25 mm and 50 mm. It was observed that there was a large areal extent (many thousands of km^2) of heavy rainfall patterns in most of the

cases. In particular, in the case of the Thessaly Prefecture, a daily exceedance of 50 mm was recorded for three consecutive days while the frequency of cloud convection occurrence was present every day during the passage of the storm over this region. The maximum daily rainfall amounts that were recorded from the examined datasets were 191 to 491 mm, according to Table 1.

In the case of Libya, where the areal extent of the rainfall patterns was relatively small (on the lower end of the mesoscale), the dynamics of the cloud convection (e.g., humid air, direction of movement, etc.) appeared to be sufficient to cause flooding. For instance, the previous days (9 September 2023 and 10 September 2023 in Figure 5f and Figure 5g, respectively) featured organized quasi-stationary cloud convection over the Mediterranean Sea, which enriched the atmosphere with large amounts of humidity and produced heavy rainfall on 10 September 2023 and 11 September 2023 over the western coast of Libya (city of Derna). Conclusively, the cloud system over the Libyan coastline, although smaller than the previous hours/days (Figure 5g,h), was convective in nature (Figure 2g,h), so it was capable of producing heavy rainfall and the severe flooding in Derna [6]. Considering that the area of Figure 5h is included in the cloud convection occurrence shown in Figure 2h, it can be said that the rainfall over the Libyan coastline was convective in nature, capable of causing sudden and extremely violent floods, resulting in thousands of human losses as well as extended damage amounting to billions of euros [6]. At this point, it is worth mentioning that the dominant presence of cloud convection patterns (in terms of frequency of occurrence) and the persistent daily rainfall patterns above the critical value of 50 mm fit well with the flood episodes in Greece (Thessaly) and Bulgaria–Turkey (Black Sea coastline). On the contrary, the case of Libya is slightly different. The most active areas over Libya in terms of cloud convection were notably smaller (Figure 2g,h and not persistent as in the case of Thessaly (Greece). Nevertheless, as the Medicane moved from the Mediterranean Sea toward to the Libyan coastline on 10 September 2024 and 11 September 2024, it was carrying out huge amounts of humid air masses and produced extreme rainfall, over the greater coastal areas of Libya. More specifically, in Figure 2g,h (cloud convection frequency of occurrence) as well as in Figure 5g,h (daily rainfall patterns above 500 mm for all the examined datasets), the pixels of interest are concentrated mainly over the greater areas of the cities Al Bayda and Al Marj where the heavy rainfall caused extended damages. In these Figures, it can be also seen that the cloud convection was not exactly over the city of Derna where the most devastating flooding occurred; instead, it was around this area and especially along the hydrographic network of this area, which destroyed the dams nearby and finally caused this devasting flood and thousands of human losses.

On the contrary, the case of Libya is slightly different because the satellites captured the highest amount of rainfall and because the cloud convection was not exactly over the city of Derna where the most devastating flooding occurred; instead, it was around this area and especially along the hydrographic network of the area, which destroyed the dams nearby and caused this final episode.

This finding highlights that although satellite-based rainfall products can efficiently capture extreme rainfall amounts and their spatial extent, topographic information is also crucial for studying floods, especially in early-warning systems. Also, the significant amounts of rainfall that are produced by the stratiform regions of large mesoscale convective systems such medicanes and not only by the cloud regions of active convection can also cause significant flood episodes. Moreover, another important finding is the fact that although there is a small underestimation of the actual rainfall height with respect to the rain gauges in the extreme high values, as is referred to in other studies about the same storm event [4,29], satellite-based rainfall products can be valuable in capturing the rainfall patterns and highlighting the extent of the rainfall, which is crucial in early warning systems and decision making.

In contrast to this study, which relies on three satellite-based rainfall datasets to capture the extremity and duration of storm “Daniel” during a specific period, previous studies, such as those on the medicane “Ianos”, employ different approaches and satellite

instruments. For example, the study by Comellas et al., 2021 [40], focuses on data from the GPM-CO DPR and ASCAT instruments, emphasizing Ku-band reflectivity, the solid hydrometeor content, and wind estimates for a specific time during the medicane "Ianos", without considering a broader intercomparison of satellite rainfall products [40]. The study of Vourlioti et al., 2022 [41], on the other hand, employs numerical weather prediction through the WRF model with data assimilation, offering high-resolution weather forecasts for several initialization periods, which differs from our exclusive reliance on satellite remote sensing products. Finally, the study of Lagouvardos et al., 2022 [42], highlights the use of the GPM CO satellite and MSG SEVIRI data, similar to this study, but focuses on the structural analysis of the storm (including brightness, temperature and 3D precipitation structure) using complimentary ground-based weather station data [42]; this is unlike our approach, which emphasizes a comprehensive intercomparison of satellite-based rainfall estimates and depicts their unique ability to capture the spatial extents of rainfall and their accuracy in estimating rainfall amounts.

Conclusively, it is worth noting the significant role of satellite-based rainfall products in studying such extreme weather events because they can monitor, in near real-time and record with sufficient accuracy, not only the amount of rainfall but also its spatial distribution. This capability is important in improving civil protection services and enhancing early warning procedures, as well as updating relevant governmental protocols for good practices towards the holistic management of such extreme weather events.

Author Contributions: Conceptualization, S.K.; methodology, S.K.; software, S.K.; validation, S.K., and N.P.; formal analysis, S.K., and N.P.; investigation, S.K., and N.P.; resources, S.K., and N.P.; data curation, S.K., and N.P.; writing—original draft preparation, S.K.; writing—review and editing, S.K., and N.P.; visualization, S.K., and N.P.; supervision, S.K. All authors have read and agreed to the published version of the manuscript.

Funding: This research received no external funding.

Institutional Review Board Statement: Not applicable.

Informed Consent Statement: Not applicable.

Data Availability Statement: The raw data were used can be found in the official site of EUMETSAT about the HSAF datasets (https://www.eumetsat.int/search?text=HSAF accessed on 16 may 2024) and NASA GES DISC about the GPM-IMERG (https://gpm.nasa.gov/data/imerg accessed on 16 may 2024) datasets. The MRP datasets presented were used in this study are experimental (part of an ongoing study to certify and capitalize their accuracy) and available on request from the corresponding author due to the national legislation and the host institution policy which have limitations about the official public availability of research data products which related with physical disasters.

Acknowledgments: The authors acknowledge the relative agencies and organizations regarding the provision of the datasets used in this study: EUMETSAT (European Organization for the Exploitation of Meteorological Satellites) for the free provision of the Meteosat multispectral satellite images (raw datasets). Also, the authors acknowledge the United Kingdom's Meteorological Office, known as "Met Office" (https://www.metoffice.gov.uk/) (accessed on 23 May 2024) for the provision of free daily synoptic surface weather maps. Finally, the authors acknowledge the NASA/Goddard Space Flight Center's (archived at the NASA GES DISC) for the free provision of GPM-IMERG datasets.

Conflicts of Interest: The authors declare no conflicts of interest.

References

1. IPCC. *Climate Change 2023: Synthesis Report*; Contribution of Working Groups I, II and III to the Sixth Assessment Report of the Intergovernmental Panel on Climate Change; Core Writing Team, Lee, H., Romero, J., Eds.; IPCC: Geneva, Switzerland, 2023; 184p. [CrossRef]
2. Dobrovičová, S.; Dobrovič, R.; Dobrovič, J. The Economic Impact of Floods and their Importance in Different Regions of the World with Emphasis on Europe. *Procedia Econ. Financ.* **2015**, *34*, 649–655. [CrossRef]
3. Pizzorni, M.; Innocenti, A.; Tollin, N. Droughts and Floods in a Changing Climate and Implications for Multi-Hazard Urban Planning: A Review. *City Environ. Interact.* **2024**, *24*, 100169. [CrossRef]

4. Dimitriou, E.; Efstratiadis, A.; Zotou, I.; Papadopoulos, A.; Iliopoulou, T.; Sakki, G.-K.; Mazi, K.; Rozos, E.; Koukouvinos, A.; Koussis, A.D.; et al. Post-Analysis of Daniel Extreme Flood Event in Thessaly, Central Greece: Practical Lessons and the Value of State-of-the-Art Water-Monitoring Networks. *Water* **2024**, *16*, 980. [CrossRef]
5. United Nations Satellite Centre (UNOSAT). *10 September 2023 Mediterranean Sea Storm Daniel in Libya, Preliminary Satellite-Based Comprehensive Damage Assessment Report*; East Province, Libya; UNOSAT: Geneva, Switzerlan, 2023. Available online: https://unosat.org/static/unosat_filesystem/3687/UNOSAT_Preliminary_Comprehensive_DA_Report_September2023_FL20230912LBY.pdf (accessed on 1 January 2024).
6. Normand, J.; Heggy, E. Assessing Flash Flood Erosion Following Storm Daniel in Libya. *Nat. Commun.* **2024**, *15*, 6493. [CrossRef]
7. Lehmkuhl, F.; Schüttrumpf, H.; Schwarzbauer, J.; Brüll, C.; Dietze, M.; Letmathe, P.; Völker, C.; Hollert, H. Assessment of the 2021 Summer Flood in Central Europe. *Environ. Sci. Eur.* **2022**, *34*, 107. [CrossRef]
8. Tradowsky, J.S.; Philip, S.Y.; Kreienkamp, F.; Kew, S.F.; Lorenz, P.; Arrighi, J.; Bettmann, T.; Caluwaerts, S.; De Cruz, L.; de Vries, H.; et al. Attribution of the Heavy Rainfall Events Leading to Severe Flooding in Western Europe during July 2021. *Clim. Change* **2023**, *176*, 90. [CrossRef]
9. Meyer, J.; Neuper, M.; Mathias, L.; Zehe, E.; Pfister, L. Atmospheric Conditions Favouring Extreme Precipitation and Flash Floods in Temperate Regions of Europe. *Hydrol. Earth Syst. Sci.* **2022**, *26*, 6163–6183. [CrossRef]
10. Ludwig, P.; Ehmele, F.; Franca, M.; Mohr, S.; Caldas-Alvarez, A.; Daniell, J.; Ehret, U.; Feldmann, H.; Hundhausen, M.; Knippertz, P.; et al. A Multi-Disciplinary Analysis of the Exceptional Flood Event of July 2021 in Central Europe—Part 2: Historical Context and Relation to Climate Change. *Nat. Hazards Earth Syst. Sci.* **2023**, *23*, 1287–1311. [CrossRef]
11. Hong, Y.; Adler, R.F.; Negri, A.; Huffman, G.J. Flood and Landslide Applications of Near Real-Time Satellite Rainfall Products. *Nat. Hazards* **2007**, *43*, 285–294. [CrossRef]
12. Nobre, G.G.; Jongman, B.; Aerts, J.; Ward, P.J. The Role of Climate Variability in Extreme Floods in Europe. *Environ. Res. Lett.* **2017**, *12*, 084012. [CrossRef]
13. Nikolopoulos, E.I.; Anagnostou, E.N.; Borga, M. Using High-Resolution Satellite Rainfall Products to Simulate a Major Flash Flood Event in Northern Italy. *J. Hydrometeorol.* **2013**, *14*, 171–185. [CrossRef]
14. Ma, M.; Wang, H.; Jia, P.; Tang, G.; Wang, D.; Ma, Z.; Yan, H. Application of the GPM-IMERG Products in Flash Flood Warning: A Case Study in Yunnan, China. *Remote Sens.* **2020**, *12*, 1954. [CrossRef]
15. Pan, X.; Wu, H.; Chen, S.; Nanding, N.; Huang, Z.; Chen, W.; Li, C.; Li, X. Evaluation and Applicability Analysis of GPM Satellite Precipitation over Mainland China. *Remote Sens.* **2023**, *15*, 2866. [CrossRef]
16. Di Paola, F.; Ricciardelli, E.; Cimini, D.; Romano, F.; Viggiano, M.; Cuomo, V. Analysis of Catania Flash Flood Case Study by Using Combined Microwave and Infrared Technique. *J. Hydrometeorol.* **2014**, *15*, 1536–1545. [CrossRef]
17. Varlas, G.; Anagnostou, M.N.; Spyrou, C.; Papadopoulos, A.; Kalogiros, J.; Mentzafou, A.; Michaelides, S.; Baltas, E.; Karymbalis, E.; Katsafados, P. A Multi-Platform Hydrometeorological Analysis of the Flash Flood Event of 15 November 2017 in Attica, Greece. *Remote Sens.* **2019**, *11*, 45. [CrossRef]
18. Munawar, H.S.; Hammad, A.W.A.; Waller, S.T. Remote Sensing Methods for Flood Prediction: A Review. *Sensors* **2022**, *22*, 960. [CrossRef]
19. Amitrano, D.; Di Martino, G.; Di Simone, A.; Imperatore, P. Flood Detection with SAR: A Review of Techniques and Datasets. *Remote Sens.* **2024**, *16*, 656. [CrossRef]
20. Sajjad, A.; Lu, J.; Aslam, R.W.; Ahmad, M. Flood Disaster Mapping Using Geospatial Techniques: A Case Study of the 2022 Pakistan Floods. *Environ. Sci. Proc.* **2023**, *25*, 78. [CrossRef]
21. Wu, H.; Adler, R.F.; Hong, Y.; Tian, Y.; Policelli, F. Evaluation of Global Flood Detection Using Satellite-Based Rainfall and a Hydrologic Model. *J. Hydrometeorol.* **2012**, *13*, 1268–1284. [CrossRef]
22. Chintalapudi, S.; Sharif, H.; Xie, H. Sensitivity of Distributed Hydrologic Simulations to Ground and Satellite-Based Rainfall Products. *Water* **2014**, *6*, 1221–1245. [CrossRef]
23. Retalis, A.; Katsanos, D.; Tymvios, F.; Michaelides, S. Comparison of GPM IMERG and TRMM 3B43 Products over Cyprus. *Remote Sens.* **2020**, *12*, 3212. [CrossRef]
24. Datti, A.D.; Zeng, G.; Tarnavsky, E.; Cornforth, R.; Pappenberger, F.; Abdullahi, B.A.; Onyejuruwa, A. Evaluation of Satellite-Based Rainfall Estimates against Rain Gauge Observations across Agro-Climatic Zones of Nigeria, West Africa. *Remote Sens.* **2024**, *16*, 1755. [CrossRef]
25. Dinku, T.; Ceccato, P.; Connor, S. Challenges to Satellite Rainfall Estimation over Mountainous and Arid Parts of East Africa. *Int. J. Remote Sens.* **2011**, *32*, 5965–5979. [CrossRef]
26. Palharini, R.; Vila, D.; Rodrigues, D.; Palharini, R.; Mattos, E.; Undurraga, E. Analysis of extreme rainfall and natural disasters events using satellite precipitation products in different regions of Brazil. *Atmosphere* **2022**, *13*, 1680. [CrossRef]
27. Palharini, R.S.A.; Vila, D.A.; Rodrigues, D.T.; Palharini, R.C.; Mattos, E.V.; Pedra, G.U. Assessment of extreme rainfall estimates from satellite-based: Regional analysis. *Remote Sens. Appl. Soc. Environ.* **2021**, *23*, 100603. [CrossRef]
28. Taye, M.; Mengistu, D.; Sahlu, D. Performance evaluation of multiple satellite rainfall data sets in central highlands of Abbay Basin, Ethiopia. *Eur. J. Remote Sens.* **2023**, *56*, 2233686. [CrossRef]
29. He, K.; Yang, Q.; Shen, X.; Dimitriou, E.; Mentzafou, A.; Papadaki, C.; Stoumboudi, M.; Anagnostou, E. Brief communication: Storm Daniel flood impact in Greece in 2023: Mapping crop and livestock exposure from synthetic-aperture radar (SAR). *Nat. Hazards Earth Syst. Sci.* **2024**, *24*, 2375–2382. [CrossRef]

30. Kolios, S. Hail Detection from Meteosat Satellite Imagery Using a Deep Learning Neural Network and a New Remote Sensing Index. *Adv. Space Res.* **2023**, *72*, 3009–3021. [CrossRef]
31. Kolios, S.; Feidas, H. A Warm Season Climatology of Mesoscale Convective Systems in the Mediterranean Basin Using Sat-ellite Data. *Theor. Appl. Climatol.* **2010**, *102*, 29–42. [CrossRef]
32. HSAF. Product H61B: Product User Manual. Available online: https://hsaf.meteoam.it/Products/Detail?prod=H61B (accessed on 23 July 2024).
33. Huffman, G.J.; Bolvin, D.T.; Braithwaite, D.; Hsu, K.; Joyce, R.; Kidd, C.; Nelkin, E.J.; Sorooshian, S.; Tan, J.; Xie, P. *Algorithm Theoretical Basis Document (ATBD) for Version 06 of NASA Global Precipitation Measurement (GPM) Integrated Multi-satellitE Retrievals for GPM (IMERG)*; Global Precipitation Measurement (GPM), National Aeronautics and Space Administration (NASA): Greenbelt, MD, USA, 2020.
34. Adler, R.; Huffman, G.; Behrangi, A. New Version 3 of Monthly and Daily Global Precipitation Climatology Project Data. *GEWEX Quart.* **2022**, *32*. Available online: https://www.gewex.org/gewex-content/files_mf/1656511026Q22022.pdf (accessed on 23 July 2024).
35. Kolios, S.; Hatzianastasiou, N.; Lolis, C.J.; Bartzokas, A. Accuracy Assessment of a Satellite-Based Rain Estimation Algorithm Using a Network of Meteorological Stations over Epirus Region, Greece. *Atmosphere* **2022**, *13*, 1286. [CrossRef]
36. Mahmoud, M.T.; Al-Zahrani, M.A.; Sharif, H.O. Assessment of Global Precipitation Measurement Satellite Products over Saudi Arabia. *J. Hydrol.* **2018**, *559*, 1–12. [CrossRef]
37. Faradiba, F. Analysis of Intensity, Duration, and Frequency Rain Daily of Java Island Using Mononobe Method. *J. Phys. Conf. Ser.* **2021**, *1783*, 012107. [CrossRef]
38. Wang, W.; Hocke, K.; Matzler, C. Physical Retrieval of Rain Rate from Ground-Based Microwave Radiometry. *Remote Sens.* **2021**, *13*, 2217. [CrossRef]
39. Alahacoon, N.; Edirisinghe, M.; Ranagalage, M. Satellite-Based Meteorological and Agricultural Drought Monitoring for Agricultural Sustainability in Sri Lanka. *Sustainability* **2021**, *13*, 3427. [CrossRef]
40. Comellas Prat, A.; Federico, S.; Torcasio, R.C.; D'Adderio, L.P.; Dietrich, S.; Panegrossi, G. Evaluation of the Sensitivity of Medicane Ianos to Model Microphysics and Initial Conditions Using Satellite Measurements. *Remote Sens.* **2021**, *13*, 4984. [CrossRef]
41. Vourlioti, P.; Mamouka, T.; Agrafiotis, A.; Kotsopoulos, S. Medicane Ianos: 4D-Var Data Assimilation of Surface and Satellite Observations into the Numerical Weather Prediction Model WRF. *Atmosphere* **2022**, *13*, 1683. [CrossRef]
42. Lagouvardos, K.; Karagiannidis, A.; Dafis, S.; Kalimeris, A.; Kotroni, V. Ianos—A Hurricane in the Mediterranean. *Bull. Am. Meteorol. Soc.* **2022**, *103*, E1621–E1636. [CrossRef]

Disclaimer/Publisher's Note: The statements, opinions and data contained in all publications are solely those of the individual author(s) and contributor(s) and not of MDPI and/or the editor(s). MDPI and/or the editor(s) disclaim responsibility for any injury to people or property resulting from any ideas, methods, instructions or products referred to in the content.